Presented at the 1978 IEEE Nuclear Science Symposium, Washington, D. C., October 18-20, 1978

AN IMAGING INSTRUMENT FOR POSITRON EMITTING HEAVY ION BEAM INJECTION

Jorge Llacer, Aloke Chatterjee, Horace C. Jackson, Jaff C. Lin and Maria V. Zunzunegui

October 1978

Prepared for the U. S. Department of Energy under Contract W-7405-ENG-48

emitted λ-ray pairs in coincidence for a distance of 10 cm between planes, or 22,800 cts/min-μCi, assuming no energy discrimination and no substantial scattering. Initial simulations also showed that efficiency would depend approximately as the reciprocal of distance between detector planes. As the distance increases, the γ-rays can penetrate the crystals in a direction closer to longitudinal. The increased detector efficiency compensates, in part, for the $1/r^2$ solid angle dependence. For a distance of 3 cm between crystal centers, a length of 9 cm along the ion-beam axis is covered.

It was also decided that each row of four detectors would constitute a detachable independent module so that the basic instrument can be used in a different or expanded configuration in the future.

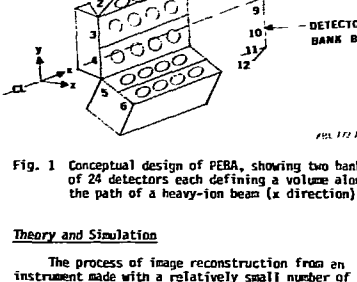

Fig. 1 Conceptual design of PEBA, showing two banks of 24 detectors each defining a volume along the path of a heavy-ion beam (x direction).

Theory and Simulation

The process of image reconstruction from an instrument made with a relatively small number of large detectors required the development of an appropriate theoretical background. A companion paper by one of the authors (J. Llacer), develops a theory of imaging for systems with a very limited number of projections. That theory has been applied to the design, simulation and actual operation of the present instrument.

Essentially, the theory shows that a detector configuration and a series of "system points" whose activity is to be determined are characterized by a real, positive, square symmetric matrix A'. The solution $\vec{x}$, the vector of unknown activities at the system points, is then given as

$$\vec{x} = \sum_{i=1}^{n} \frac{\alpha_i}{\lambda_i} \vec{x}_i \qquad (1)$$

where n is the number of system points, $\vec{x}_i$ are the eigenvectors and λ_i the eigenvalues of A'. The values α_i are the result of a mathematical projection of the results of a measurement on the $\vec{x}_i$.

The correctness of the solution $\vec{x}$ in the presence of statistical fluctuations depends on the value of the Condition Number of the matrix A'

$$C.N. = \lambda_{max}/\lambda_{min} \qquad (2)$$

A large Condition Number is not desirable.

The process of design of PEBA has required the development of a valid computer simulation procedure so that different detector configurations could be tested, the condition numbers of the resulting matrices could be evaluated, and their effect on imaging studied. The imaging objectives were defined as follows:

(i) ability to locate a point source on the ion-beam axis with an activity of 0.1 to 0.2 μCi with an accuracy of the order of 1 to 2 cm in a counting time of a few seconds;

(ii) ability to obtain the best possible quantitative information on activity as a function of time in the volume spanned by the detector planes consistent with the limited number of projections available.

The first objective involves finding the optimum relative positions in the x direction (Fig. 1) of the twelve detector modules of banks A and B (four detectors per module) so that system points on the center axis can be located very near each other and still result in a well behave matrix. The second objective required the investigation of matrices obtained from three-dimensional arrays of points. For practically in data presentation and interpretation, the array should be rectangular.

System matrices to simulate the physical system were obtained by digital calculations; the two arrays of 24 detectors were simulated with their actual dimensions in space. For a particular point source at s_j, the projections from a raster of points at the entrance surface of every detector bank A, passing through s_j and intersecting entrance surfaces of detectors of bank B, were calculated. For all lines passing through s_j that join two opposite detectors, the length of the γ-ray trajectories inside the cylindrical detectors and the corresponding probabilities of the interaction was obtained (photoelectric plus Compton). From these probabilities, it was then possible to construct a column vector of 576 elements (24 x 24) that contains as entries, the frequencies with which all possible coincidences from s_j can occur. Repeating the procedure for all system points under investigation and placing the column vectors side by side, we obtain the system matrix A. Multiplication by its transpose A^T yields the symmetric matrix A', which can then be analyzed in terms of the eigenvalues. It as expected that the simulated system would be a good representation of the physical system. The only physical phenomenon not included was the interaction in a given crystal of photons that do not enter through the entrance window of the same detector crystal. Interaction in more than one crystal of the same bank in time coincidence would be rejected electronically.

One successful configuration that would meet the design objective (i) was found and is shown in Fig. 2. The left-to-right axis is the ion-beam axis (x coordinate in Fig. 1). The projection on the (x, y) plane of the center of the detector faces is shown with + and x signs for banks A and B, respectively.

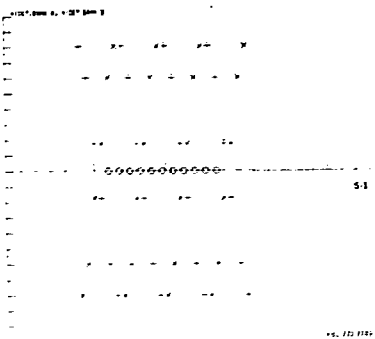

Fig. 2 Projection onto a vertical plane of detector center positions for banks A and B in a favorable configuration for maximum sampling of the center axis. A set of system points are shown by circles.

A crossed pattern between detectors in banks A and B with each row within a bank displaced 5 cm with respect to the row above (or below) results in a coincidence sampling of the center axis every 5 cm. A series of system points on the center axis is also shown in Fig. 2 by circles.

Figure 3 shows the Condition Number of the matrices generated in this arrangement as a function of Δx, the interpoint distance. Only the central 5 cm of the axis are being sampled in this study. The fast rise in $\lambda_{max}/\lambda_{min}$ for $\Delta x < 0.7$ cm is, undoubtedly, due to coupling of contiguous points caused by the large dimensions of the crystals.

Imaging simulations with different sets of system points and matrices were carried out it was determined that the first design objective could be met amply if the Condition Number was no higher than 10 to 15 for the configuration used. The Nyquist interpolation scheme described in the companion theoretical paper was used to evaluate positional accuracy.

Simulations in three dimensions were also carried out and, as expected, the very small number of projections imposed, severe limitations on imaging ability. We shall return to this point below.

General Design Considerations

The physical layout of PEBA, which was intended primarily as a test bed for physics and instrumentation ideas and for experiments with small animals is shown in Fig. 4. Three groups of 8 detectors each form the left and right banks, and each module of 4 detectors can be adjusted in its position along the beam axis independently. When the distance between

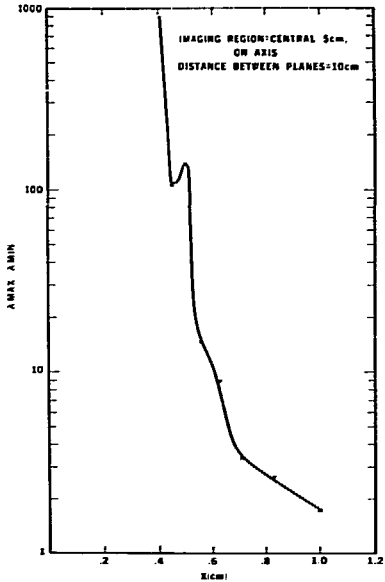

Fig. 3 Matrix condition number as a function of distance X between system points for imaging along the beam axis, in a region of 5 cm length.

detector banks is changed, the upper and lower detector groups change their angle so that all the tubes are always looking approximately towards the center line.

Electronically, each module of four tubes supplies timing, energy and tube address information to a main unit which performs coincidence/anticoincidence functions, analog to digital pulse height conversion and coincidence address generation. A microprocessor unit with an 8K 16-bit memory performs all the real time logic functions during calibration or data acquisition and communicates with a CAMAC module attached to a multi-tasking PDP-11/45 computer. The large computer issues commands (one or two 16-bit words) to PEBA, which are then executed by the microprocessor. At the end of execution, data are sent back to the 11/45 for mathematicaly processing and image display.

There are two features in the overall design philosophy which should be mentioned:

becomes a column of the system matrix. A three-dimensional source positioner controlled by the PEBA microprocessor has been built for that purpose. Thus, the image reconstruction process uses different matrices A' for different distances between detector planes and/or different sets of system points.

Detector Module and Main Unit Design

A block diagram illustrating the main function of the main unit is shown in Fig. 5. This diagram for the "A" bank of detectors is mirrored by a similar block diagram for the "B" bank of detectors. The digital and analog signals (DS and AS) are processed in the two respective cards, with the digital card controlling the flow of information in the analog card. Also, the photomultiplier tube (PMT) address is forced on the digital card as a 5-bit word. The analog signal is converted by an 8-bit analog-to-digital converter (ADC) contained on the analog card. The digital information is then combined into one 13-bit word in the control card and sent to the microprocessor (μP).

Fig. 4 Layout of PEBA, showing the 24 tubes of one detector bank arranged in modules of four detectors each.

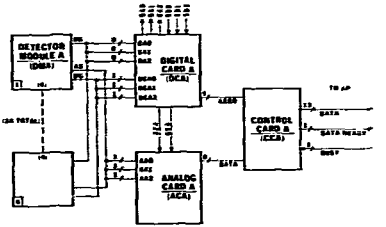

Fig. 5 Diagram showing the function of the main electronic unit of PEBA.

1) Energy selection is done by the PEBA microprocessor without need to keep PM tube gains identical. Instead, PM tube voltage is adjusted for optimum coincidence timing performance (30 nsec FWHM for the complete system). In a calibration mode, pulse height analysis spectra of 24 tubes at a time is carried out by the PEBA microprocessor system, and a table of lower and upper channel numbers (0-255) bounding the energy window allowed for each tube address is prepared. During the normal data acquisition mode, the microprocessor consults the table stored in its own memory to see whether the pulse height of the two tubes involved in a coincidence is within the prescribed bounds or not, thus accepting or rejecting the event. For the TI 9900 processor used, the operation of checking four bounds takes 250 μsec, which may be acceptable for low activity levels, but a hardware implementation has been nearly completed which does the checking in 4 μsec.

2) The generation of system matrices for a specific geometry is done under computer control by taking a point source (^{22}Na) embedded in plastic and physically placing it at the system points in succession. After counting a prescribed length of time, the resulting vector of responses from each point

The PMTs used are RCA C70042Y, which are 10 stage tubes with a 0.75" (1.91 cm) diameter bialkali photocathode. These PMTs were chosen with regard to their performance/cost ratio. Here the performance criteria included:

a) amplitude resolution - fullwidth at half-maximum for ^{22}Na was measured at ~15% with NaI detectors, 0.75" diameter, 3" long.

b) peak shift with counting rate - this was <2% for the range of cps to 300,000 cps.

c) timing resolution - using simple leading edge discrimination and a time-to-height converter, with a ^{22}Na source this was ~8 nsec fullwidth at half-maximum (16 nsec FW 0.1M).

The basic elements of the detector module design are shown in Fig. 6. A fast timing signal is taken from the anode of the PMT and an analog signal is obtained from the last dynode. The wave forms shown in the figure are typical for a source of ^{22}Na with ~1000 V applied to the PMT. The CD4016 is a COS/MOS bilateral switch that is normally open but is closed by a tice coincidence of the DS signals from the "A" and "B" detector banks, indicative of positron annihilation.

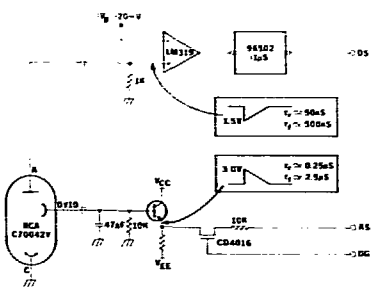

Fig. 6 Basic elements of the detector module design.

Each detector module consists of four PMTs and two circuits cards; one containing four digital channels and the other four analog channels. This construction keeps the large fast digital signals separate from the smaller and slower analog signals.

The basic logic contained on the digital card is shown in Fig. 7. In Fig. 7(a) the digital signals (DS) from a segment of eight PMTs are first differentiated to be ~20 nsec wide by a leading edge shaper and then combined in an 8-input OR gate to form the segment signal SA0. In a similar manner, digital signals A8-A15 are combined to form SA1, and A16-A23 form SA2. Likewise, the digital signals from the "B" bank of detectors are combined to form SB0, SB1 and SB2. A positron annihilation is determined by a tice coincidence of any one of the DSA signals with a DSB signal at the 74S00 NAND gate. The 9602 multivibrator at the output of the 74S00 will trigger with an overlap of the timing signals ≥3-4 nsec. With a positron identified, all dynode gates of one particular segment in both "A" and "B" banks are closed for ~0.6 μsec. Simultaneously, another 9602 generates a 6.0 μsec pulse. This is the gate (SG) for the stretcher circuit that is located on the analog card.

Now it is always possible for the annihilation radiation from one positron decay to be indicated in two adjacent digital channels. This would give rise to faulty addressing of the PMT. A veto signal is

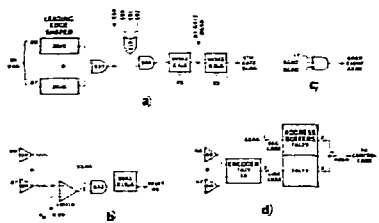

Fig. 7 Details of the logic on the digital cards.

therefore included as shown in Fig. 7(b). A simple summing amplifier is used to form a >1 signal, which in coincidence with a DG signal, triggers a 9602 to form a reset signal (RS) that immediately clears the dynode and stretcher gate multivibrators. A good event (GE) is formed at the back edge of the DG signal as shown in Fig. 7(c). The 0.6 μsec delay is to allow the >1 signal to form if necessary. The address of a good event is determined by segment (1 of 3) and line (1 of 8), which are combined to form a 5-bit address as shown in the basic address circuit of Fig. 7(d).

The basic circuits of the analog card are shown in Fig. 8. The analog signals, combined as one of three segments, are connected from the detector module to the main unit by 50 Ω coax cable for shielding purposes. At the analog card, the three segment analog signals are summed at the input of an inverting amplifier. Recall only one segment dynode gates would have been activated. In the stretcher circuit the amplitude of the signal from the LM318 is stored on a stretching capacitor for a time determined by the stretcher gate signal (SG). The voltage gain of the analog channel from the PMT dynode to the output of the stretcher circuit is ~1.0. With a good event indicated, another COS/MOS bilateral switch is activated and the analog signal is processed by the 8-bit ADC.

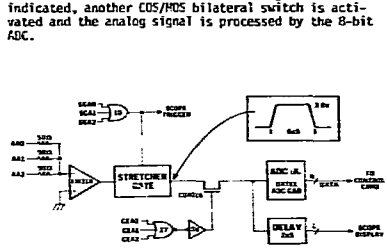

Fig. 8 Basic circuits in the analog cards.

Additional features not shown in these circuit diagrams are the ability to override the >1 veto signal by the simple closure of a toggle switch. Also, by use of a toggle switch, the fast coincidence gate on the digital card may be converted to process single events.

Microprocessor Unit Design

The general configuration of the μP unit used in PEBA is shown in Fig. 9. The main chip used in the unit is the TMS 9900 16-bit word microprocessor manufactured by TI. The unit also contains: 2K of EPROMS (2708) for program storage; 2K of static RAMS (SEMI 4200) for data storage; several serial I/O channels (CRU channels); a DMA channel which is used for data acquisition from the detector unit; seven interrupt levels and other logic for executing several specific PEBA commands.

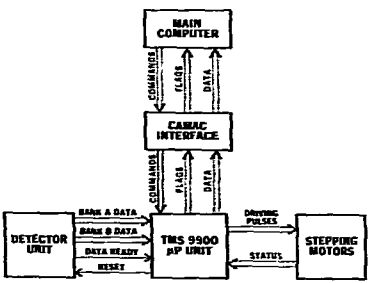

FBL 788-9577

Fig. 9 General configuration of the microprocessor unit used in PEBA.

The PEBA commands can be divided into two categories: a) motor movement commands, b) data collection commands. A command can be either one word or two words. The MSB of the first command word must always be a "one" which is sensed by the hardware as an indicator to start the program. Once the program is started, it decodes the command and branches to respective routines.

a) Motor movement commands: when a motor movement command is decoded, a timer and an interrupt level are used for sending the driving pulses. No other hardware is involved in motor driving. All pulse generation is controlled by software.

In each direction, for every step moved, the shaft encoder in the motor unit echoes back to the μP a signal to trigger an interrupt routine which records the actual number of steps moved. When all the motors stop, the μP sends the total number of steps to the main computer as a reference.

b) Data collection commands: the four commands in this category will be described in some detail.

SS (Bank, tube count) (Store Spectrum): this command is used for gathering energy spectra from either bank "A" or bank "B" for calibration purposes. The command specifies the bank, the monitor tube and the number of total counts desired in the monitor tube. While the memory is doing the pulse height analysis by taking the data from a complete bank of detectors through the DMA channel, the μP unit filters all the counts through hardware and routes only those from the monitor tube into a counter. When the counter is full, the μP senses it and stops the operation. Because the RAM size limitations, the SS command can only be executed one bank at a time.

RS (bank, tube) (Read Spectrum): this command reads out the pulse height spectrum of the specified tube obtained during SS operation. The 256-word spectrum is transferred to the main computer.

SB (Send Boundary): this command allows the main computer to send the lower and upper channel number for each tube that will be used for energy selection in the XV command. The μP stores these bounds in a block in its RAM.

XV (n, ΔT) (Generate Experimental Vector): this command asks the μP to generate a vector of coincidences for each period ΔT, repeat n times, and sending each vector to the main computer with double buffering. Whenever a coincidence occurs between bank "A" and "B", the μP strobes the two 13-bit (5 tube-address bits and 8 data bits) detector unit output into two registers. The hardware then generates a sequence to fetch the lower and upper bounds for the two tubes involved in the event, and compares the data with these bounds. If both the two 8-bit data are within the lower-upper bounds a "Good Event" signal is generated which then rearranges the two 5-bit tube address into a 10-bit word and route them into the DMA channel to generate an event spectrum. A timer is used to define the time frame.

Algorithms and Displays

Two methods have been used for solving the basic system equation

$$A' \vec{x} = \vec{k}' \qquad (3)$$

where A' is the symmetric matrix, $\vec{x}$ is the unknown vector of activities and $\vec{k}'$ is a rotated vector of experimental results. The first one is a direct solution to Eq. 3 by the conjugate gradient method, which is guaranteed to arrive at the best solution in the least-squares sense. Calculations in 32-bit floating point arithmetic take a maximum of 0.3 sec for one-dimensional problems with up to 10 system

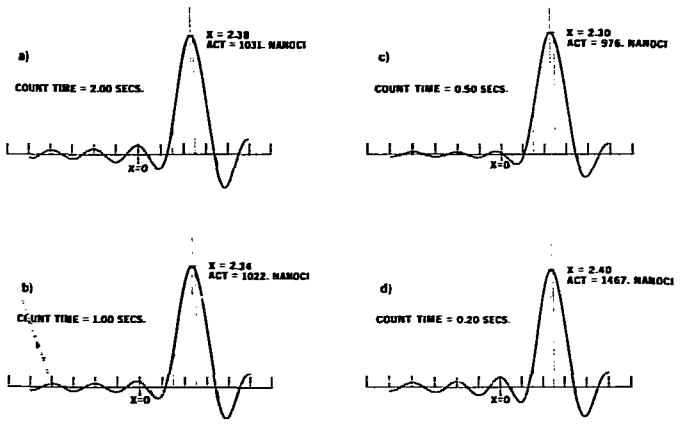

Fig. 10 Example of point source detection in one dimension. A 1 μCi source was positioned arbitrarily at x=2.35 cm, and the unit was activated for 2, 1, 0.5 and 0.2 sec. Resulting point source position and activity are shown in each case. The Nyquist interpolation technique was used in the generation of the images.

points and 5-10 sec for three-dimensional arrays with up to 40-50 points on a PDP 11/45 computer.

The second method used is a direct application of Eq. 1 using eigenvalues and eigenvectors. The accurate determination of eigenvalues and eigenvectors from the system matrices used with PEBA does not present any apparent problems, although only 32-bit floating point arithmetic has been utilized. The solution method consists in a single pass and involves no divisions during execution time. (The $\vec{x}$ having been previously divided by the λ_{ii}.) This method seems very promising for image reconstruction work using fast array processor which do not have hardwired dividers.

Several display methods have been tried during the course of this work. The ones shown here are line drawings from a Tektronix 4014 terminal for one-dimensional work as copied by a Versatec printer-plotter and level of gray modulation displays obtained from a Versaplot software package with nine levels. A video-type color display is now being developed as the principal display method. Figures 10a) through d) were obtained from the video display in some initial test in black and white. Image interpolation between system points has been done by using the Nyquist sampling theorem. Image generation by mathematical sweeping, as described in the companion paper, and image improvement by point response deconvolution is in the process of study.

One-Dimensional Experimental Results

A) Point Source Detection

A large number of experiments have been carried out in order to determine the capabilities of the first PEBA design. The simplest series of tests consists in the determination of position and activity of a point source placed along the beam axis (x-axis) as a function of detector plane separation, counting time energy window, position and the presence of absorbers.

Figures 10 a) through d) show a set of results obtained by the iterative solution to Eq. 3 and the Nyquist interpolation technique for a 1 μCi point source positioned arbitrarily at x = +2.35 cm. Count times were 2, 1, 0.5 and 0.2 sec, with 25 cm detector plane separation, no absorber and an energy window from 25 to 124% of the photopeak centroid. Such energy window removes the Pb x-rays from the detector shields and most of the effects due to the high-energy γ-rays from the source. Figures 10 a) through d) contain the x-axis, with marks every cm. Eight system points were placed between $-3.5 \leq x \leq 3.5$ cm, every cm.

The values obtained for activity at the system points are shown by light lines. The solid curve is the result of the Nyquist interpolation. Error in position determination remains within 1 mm and activity measurement within 3% except for the lowest count time, where the error becomes substantial. Some values of x at the system points exhibit negative values due to "ringing" in the solution, magnified by the Nyquist interpolation scheme, as discussed in the theoretical paper. The ^{22}Na point source (estimated to be approximately of 1 mm diameter) emits positrons with an end point energy of 0.54 MeV, so that the source generates coincidence γ-rays from a sphere of approximately 2 mm maximum radius in lucite or water. A two-dimensional projection of the effective source distribution shows that activity decays almost linearily from the center to the edge of a circle of 2 mm radius,[5] so that the ^{22}Na source can thus be used as a reasonable point source for camera studies.

Table 1 shows a comparison between the condition numbers of the system matrices calculated by the simulation programs and the ones generated by PEBA as a function of detector plane separation for the eight system points described above.

Table 1

Plane Separation	Condition Numbers	
d (cm)	Calculated Matrix	Measured Matrix
15	1.94	3.24
25	2.12	3.78
35	2.34	3.71

From the use of the theoretical developments in the companion paper and an observation of the matrices resulting from the calculations and the measurements, it has become clear that the differences shown in Table 1 are due to a higher degree of coupling or detector response overlap in the experimental setup than in the simulation.

Evidently, this is due to the assumption made in the simulation that only γ-rays entering through the detector face are counted by the system. These comparisons and other similar ones establish the validity of the computer simulation procedure.

A statistical analysis of data collected by PEBA under conditions resembling clinical use has been carried out in order to ascertain the effect on imaging accuracy of four principal variables: 1) data collection time, 2) energy window width, 3) separation between system points, and 4) source position along the x-axis. A 1 μCi ^{22}Na source was placed in an approximately 22.5 cm diameter cylindrical water tank with plastic walls. The distance between detector banks was 35 cm. The number of coincidence events detected before energy discrimination was approximately 50 sec^{-1} (the rate is near 250 sec^{-1} without the water tank). The results to be examined were obtained location and activity of the point source.

For a fixed data collection time, t_α, an analysis of the variance was carried out for two energy windows (25% to 125% of photopeak centroid and 85% to 115%, wide and narrow, respectively), system points separated by three distances (1.5, 1 and 0.75 cm), and source positioned in three regions ($x = 0$, $1 < x < 2$ cm, and $x = 3$ cm). Each measurement was repeated six times, for a total of 108 measurements for a given t_α.

The statistical analysis shows that for images generated with 650 or less events (accepted coincidences within a prescribed energy window), accuracy in position and activity determination is limited by the random fluctuations in the collected counts. The effects of energy window width, system point separation and region of source position are not significant under those conditions.

For images generated with 1600 events or more, the analysis shows:

1) window width is not important in determining position of a source for a fixed number of accepted events. Also, as long as the system matrices are generated in the same conditions of absorber and window widths as during data taking, accuracy in activity measurement is independent of window width.

2) the camera is significantly more accurate in the center and near center regions than at the edges for a fixed counting time and window width.

3) the system with point separation of 0.75 cm gives significantly worse accuracy than in the cases with $\Delta x = 1$ or 1.5 cm, for a fixed number of events.

The first result may be somewhat surprising, even bearing in mind that when a system matrix is generated with a given set of window and absorber conditions, the matrix already contains all the relevant Compton scattering information for detection under similar conditions. This result will be investigated further. The second result is quite understandable considering that fewer tubes are recording coincidences when the source is at the edges of the camera. The third result is a consequence of the higher condition number of the matrices for $\Delta x = 0.75$ (between 6 and 7.7) than for $\Delta x = 1$, or 1.5 cm (between 1.7 and 2.6).

From the above study, we have fixed operating conditions for the camera in the presence of the water phantom as:

1) wide window (25 to 125% of photopeak centroid).

2) operate preferentially within $\pm$2.5 cm of center.

3) use system points generated with $\Delta x = 1$ cm.

With the above parameters and a short counting time, the mean error in position and activity at system points and the estimated standard deviation of the expected errors are given in Table 2.

The mean errors should be near zero except for systematic errors. The standard deviations indicate that in 68% of independent measurements the error expected will be less than σ, in 95% of measurements it will be less than 2σ, etc.

Table 2

Count Time (secs)	Accepted Events	Position (cm)		Activity (nanoCi, for 1 μCi source)	
		$\bar{e}$	σ	$\bar{e}$	σ
>20	>650	.01	±.015	4.1	±78
10	325	.006	±.039	13.6	±120
5	162	.003	±.047	40.11	±164

B) Measurements of High-Energy Heavy-Ion Range

One of the principal uses of PEBA is the on-line determination of the end point of the trajectory of heavy ions during radiation therapy. Figure 11 shows a curve of relative energy deposited per unit length (Bragg curve) by a beam of ^{12}C ions in H_2O with an initial energy of 254 MeV/nucleon. The sharp peak (Bragg peak) at the end of the trajectory determines the region of high cell damage, so that the on-line visualization of its exact position in a patient is of great importance.

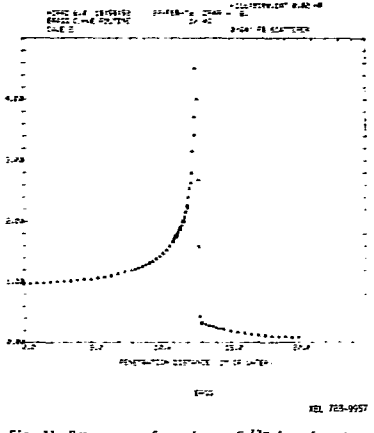

XBL 783-9957

Fig. 11 Bragg curve for a beam of ^{12}C ions in water, with initial energy of 254 MeV/nucleon.

Several experiments have been conducted at the Bevalac in order to test the ability of PEBA to detect trajectory endpoint, as well as isotope identification. Figure 12 shows a schematic of the general geometry used in the experiments. A beam of high-energy ions was collimated to a diameter of 1.52 cm (PEBA's diameter of good positional accuracy is 2 cm) and made to enter an absorber bar positioned between the detector banks, centered along the beam axis, with the x = 0 point of PEBA at some determined point.

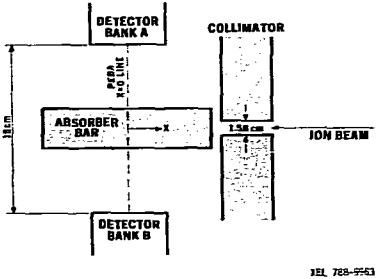

XBL 783-9953

Fig. 12 General geometrical setup for experiments with PEBA in the irradiation chamber.

Immediately after the end of the ion bombardment PEBA would start data acquisition for a number of periods of predetermined length. Data analysis and display is carried out immediately after data acquisition ends.

One of the simplest experiments that can be done is by irradiating a Beryllium target with a beam of ^{12}C particles and measuring the range in the same target of the ^{11}C particles obtained as a fragmentation product of the parent beam. The yield of ^{11}C is of approximately 1%.

For the ^{12}C beam corresponding to Fig. 11, Fig. 13 shows a graph of end-of-range peak position and detected activity vs time as measured by PEBA. The horizontal axis is the x-coordinate of PEBA in cm. Times T correspond to the beginning of a 50 sec counting period, each line representing a new period. The density of the image corresponds to activity detected. The inserted values of x correspond to peak position. From the geometry of the specific experiment, the measured range of ^{11}C generated in the Be bar is 7.45 cm ±.04 cm. A calculated value for that range is 7.85 ±0.31 cm.

A least squares linear fitting to the logarithm of detected activities in order to determine the half-life of the isotope gives a result of 21.8 minutes, which compares well with the half-life of ^{11}C, 20.5 minutes. The maximum activity detected of approximately 70 nanoCi correspond to a maximum of 1590

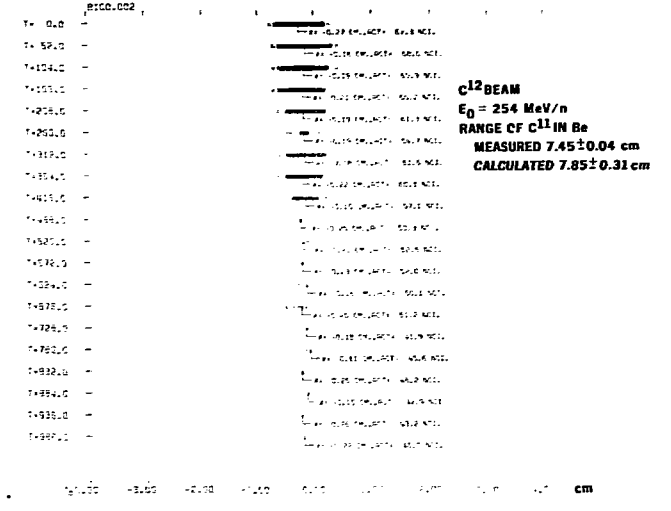

XBL 782-9958

Fig. 13 Measurement of range and half-life of ^{11}C produced by fragmentation of a ^{12}C beam in Be. The horizontal axis represents PEBA coordinates along the x axis. Vertical position corresponds to time T (secs) since end of irradiation. Images are plotted with nine levels of grey.

disintegrations per second. Since the measured efficiency of the camera under the experimental conditions is very close to 1%, each of the images of Fig. 13 was obtained with approximately 1300 counts maximum which poses no strain to the capabilities of PEBA.

A set of more demanding measurements was made with a ^{20}Ne beam with a nominal initial energy of 425 MeV/nucleon. Figure 14 shows data obtained after such an irradiation with ^{20}Ne on a Be target, with 2 cm H_2O absorber in front. Count interval was 2 sec per image. The least squares fitting gives a half-life of 19.8 sec which identifies the isotope quite well. The range obtained was 9.34 cm ±0.12 cm with a theoretical value of 9.29 ±0.28 cm. The first image was formed with approximately 250 counts.

In a higher level irradiation, we have been able to observe a shift in the detected peak position as well as a change in the dominant half-life as the activity due to ^{19}Ne decays fast, leaving ^{17}F in the target (half-life 66 secs). No water absorber was used in the experiment. Count intervals were 2 secs. Figure 15 top portion shows the results of the measurement at early times, giving a range of 10.57 ±0.06 cm, (the theoretical value of 10.49 ±0.31 cm), with a half-life of 30.6 secs (^{19}Ne contaminated with ^{17}F). The bottom portion of Fig. 15 show the renormalized results of the same experiment at later times after irradiation. The peak position is now located at 10.85 ±0.11 cm and the least squares fitting yields a half-life of 66 secs, which identifies ^{17}F quite well. The differences in position between the trajectory end points of ^{19}Ne and ^{17}F of approximately 0.3 cm compares well with previous results.[7]

The above examples provide a sampling of the one-dimensional static imaging capability of the present camera configuration. It is felt that the accuracy with which PEBA can measure end-of-range is such that the results now obtainable should be used to refine the theoretical calculations which, at present, yield results which are not better than ±3%.

A number of experiments with phantoms and animals are now being prepared from which we hope to gain enough knowledge to allow us to use the camera with humans during treatment irradiation.

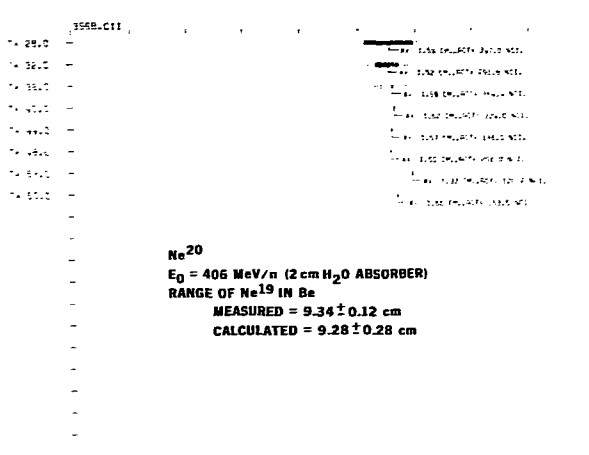

Fig. 14 Measurement of range and half-life of ^{19}Ne in Be.

Three-Dimensional Imaging

The initial computer simulations of three-dimensional imaging showed that the detector configuration used for one-dimensional imaging resulted in optimal system points located irregularly in space. At the expense of some increase in condition numbers, a rectangular mesh of system points was made a requirement. The results of the simulations and the experimental observations have coincided in pointing at the weaknesses of the structure described by Figs. 1 and 2 and 4.

1) In vertical planes (x, y), independent sampling of lines parallel to the beam axis occurs at irregular intervals Δy and condition numbers become quite high as the sampled line is moved away from the y = 0 line. The dependence on the Z coordinate is also quite strong.

2) In horizontal planes (x, z), independent sampling of lines parallel to the beam axis is very scarce, since there are no tubes in the vertical direction to complete a structure which could approach a ring.

A better geometry which has been investigated for volume reconstruction is one in which the six detector modules of each bank are stacked horizontally on top of each other. Than by positioning the modules in the (x, y) plane as shown in Fig. 16, we obtain sampling in x every 0.75 cm and in y every 1.75 cm, half of Δx and Δy shown in the figure, with no noticeable system matrix coupling in the vertical plane for a wide range of Z. Good uniformity in detector sensitivity for all the system points is observed except at the periphery of the rectangular region sampled.

A two-dimensional array of system points with NX = 9 (the number of x positions), Δx = 1, NY = 5, Δy = 1.75 cm has been investigated, covering an area of 8 x 7 cm at Z = 0. A total of 16 x 16 detectors were placed in the configuration of Fig. 17. The condition number of the matrix is 6.12 for a separation between planes of 20 cm and no absorber. In that configuration, the instrument consists virtually of 5 lines of sensitivity, parallel to the ion-beam axis, separated by 1.75 cm. For a point source traveling along the X-direction (ion-beam axis), the activity detected at a system point has a FWHM of 1.2 cm.

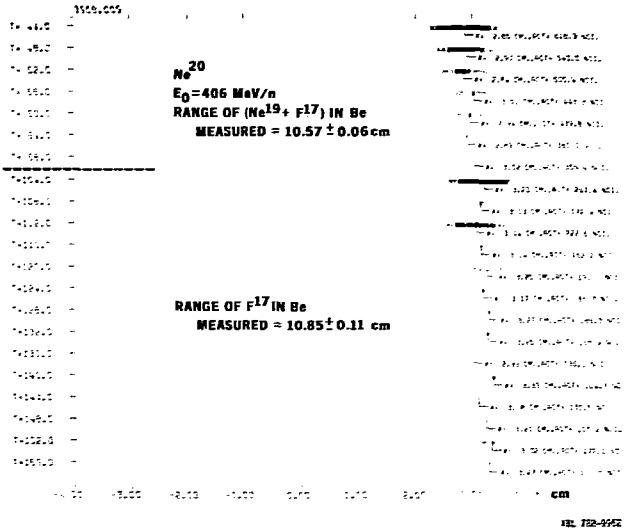

Fig. 15 Measurement showing peak shifting between ^{19}Ne and ^{17}F as the activity due to the short half-life ^{19}Ne decays, leaving the longer-lived ^{17}F in the Be bar.

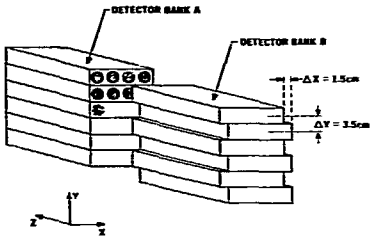

Fig. 16 A good configuration that has been investigated for imaging along nine lines in a vertical plane parallel to the beam direction. Sampling distances are 0.75 cm in the x direction, and 1.75 cm in the y direction.

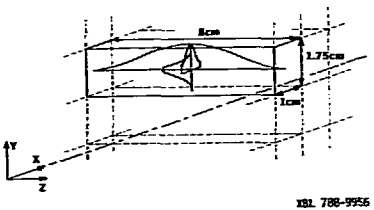

Fig. 17 Approximate definition of a picture element for the configuration of Fig. 16, showing the weighting functions that determine activity measured at a system point.

For a source traveling along the vertical axis, the corresponding response has 1.05 cm FWHM. Scans carried out by moving a source along the z-direction (horizontal, transverse to the beam), indicate that the instrument has a response of 4.8 cm FWHM, with good positional accuracy in x and y coordinates within $-4 \leq z \leq 4$ cm approximately. Figure 17 shows schematically one picture element in relationship to the beam axis with the approximate form of the weighting functions which determine the response at a system point.

Preliminary imaging experiments with the 16 x 16 detector system and the set of system points described above have been carried out. The limit of usefulness of the configuration is illustrated by an experiment in which a beam of pure ^{11}C with a range of 10.8 cm in water and a total of approximately 10^7 particles per beam pulse was used to inject that isotope into a cylinder of lucite of 3 cm diameter. After one single beam pulse, the dose delivered was approximately four rads. The number of disintegrations per second for the injected bolus of the long half-life ^{11}C is 5.6×10^3, corresponding to an activity of 150 nanoCi. In the configuration under study, the camera accepts approximately 200 counts/sec for a 1 μCi source with an energy window between 20 and 115% of photopeak, and ≈100 counts/sec for a flat distributed 1 μCi source of the shape of the bolus injected in lucite. The injected bolus was expected to generate, therefore, only 15 counts/sec in the camera, which is what was actually observed experimentally. Figure 18 shows four consecutive images obtained with 1 sec counting after the single beam pulse irradiation. The nine system point positions in the horizontally axis and the five points in the vertical axis are shown. The lucite rod was placed along the lowest horizontal system line. With an average of only 15 counts, which can result from unscattered γ-rays from the bolus, or from γ-rays Compton scattered in the lucite bar or the detectors, fluctuations in position, activity detected and the appearance of fictitious activity in the image are problems. Nevertheless, a clear point of activity is detected with rather consistent position most of the time.

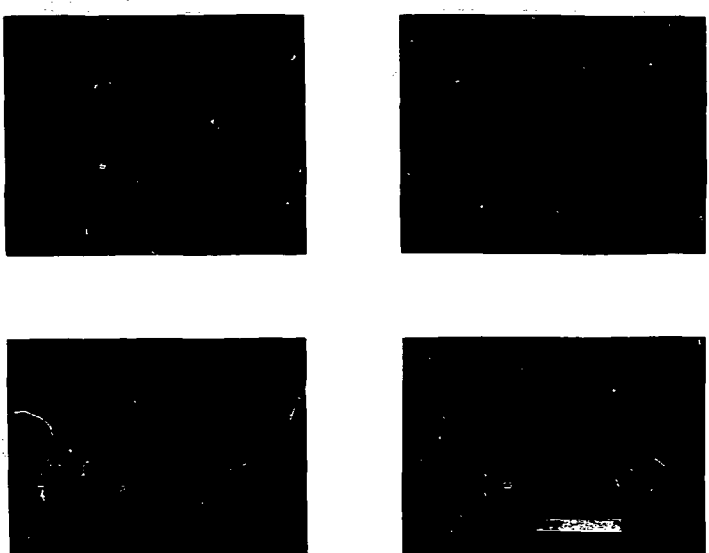

Fig. 18 Image generated by a configuration similar to that of Fig. 16 when approximately 10^7 ^{11}C ions are stopped in a plastic bar. Dose delivered was four rads. Each image corresponds to data acquired during one second, representing approximately 15 counts in the instrument. The disappearance of the point in one of the images is real and can be explained reasonably by the low count rate and the possibilities for Compton scattering in the plastic bar and/or detectors.

The use of ^{11}C for diagnostic work with humans is far from ideal, due to the long half-life of that isotope. With ^{19}Ne (half-life = 18.2 secs), a similar bolus would generate 70 times more disintegrations per second and imaging would be considerably improved. A beam of ^{19}Ne will be developed at the Bevalac in the near future.

The possibility of adding more vertical system planes at $z \neq 0$ is being investigated, although the absence of vertical detectors results in a strong coupling in the resulting matrices.

Work in both computer simulation and experimental measurements with PEBA is continuing in order to find the best way to high efficiency imaging in three-dimensions for physiological studies with injected radioactive ion beams.

Conclusion

This paper has reported on the design and initial performance data of the first version of an instrument that can determine the position of the trajectory end point of a heavy-ion beam during therapy or medical research with an accuracy of the order of 1 mm for counting times in the order of a few seconds. Using purely radioactive beams, the patient dose can be below one rad if the shorter lived position emitter isotopes are used. The instrument can also be used with some limitations, for volume activity reconstruction. This first instrument is now being used as a test bench for ideas and also for phantom and small animal experiments. It will soon be reconfigured into a more convenient mechanical unit for larger animal experiments and actual human irradiation control. Effort is continuing in the areas of optimum detector dimensions, material, packing and cluster location, on fast algorithms and system matrix generation procedures, display methods, including the concept of mathematical sweeping, and cost reduction, so that we can provide the best assistance to the Biomedical effort at LBL on cancer therapy and physiological studies.

Acknowledgments

The authors would like to recognize the strong influence on this project of C. A. Tobias, who provided the initial impetus for this work. We would also like to thank E. L. Alpen and F. S. Goulding for their interest and support.

Reference to a company or product name does not imply approval or recommendation of the product by the University of California or the U.S. Department of Energy to the exclusion of others that may be suitable.

References

1. H. A. Grunder, Lawrence Berkeley Laboratory Report LBL-2090, 1973.

2. C. A. Tobias, Radiology, 108, p. 145, 1973.

3. E. V. Benton, P. P. Henke and C. A. Tobias, Lawrence Berkeley Laboratory Report, LBL-2016, 1973.

4. F. S. Beckman, Mathematical Methods for Digital Computers, Wiley, New York, 1960.

5. J. Llacer and L. S. Graham, The Effect of Improving Energy Resolution on Gamma Camera Performance, IEEE Trans. Nucl. Sci. NS-22, No. 1, 1975, p. 309.

6. J. Alonso, LBL, private communication.

7. C. A. Tobias, A. Chatterjee, and A. R. Smith, Phys. Letter 73A, 1971, 119.